Microramp Control of Supersonic Oblique Shock-Wave/Boundary-Layer Interactions

H. Babinsky,[*] Y. Li,[†] and C. W. Pitt Ford[†]
Cambridge University, Cambridge, England CB2 1PZ, United Kingdom

The potential of microramp sub-boundary-layer vortex generators for flow control in supersonic engine inlets is investigated. In particular, the study focuses on the ability of these devices to beneficially affect oblique shock-wave/boundary-layer interactions. Experiments have been conducted at Mach 2.5 to determine the nature of flow controlled by microramps and to investigate their ability to delay separation in a reflected shock interaction. Various ramp heights between 30 and 90% of the boundary-layer thickness were investigated. The details of the vortical flow generated by such devices were identified. The general flow features were found to scale with device height and it is suggested that smaller devices need to be placed closer to the expected adverse pressure gradients. When applied to a separated oblique shock-wave/boundary-layer interaction generated with a 7 degree wedge, microramps were not able to completely eliminate flow separation, although they were shown to break up separated regions. Other performance indicators across the shock-wave/boundary-layer interaction were also improved through the application of the devices.

Nomenclature

c	=	microramp side length
H_i	=	incompressible boundary-layer shape factor δ^*/θ
h	=	microramp height
p	=	wall pressure
p_0	=	stagnation pressure in the settling chamber
s	=	device spacing
U	=	streamwise velocity
U_∞	=	boundary-layer edge velocity
U^+	=	streamwise velocity in law-of-the-wall coordinates
X	=	streamwise distance from the working-section start
X_{TE}	=	streamwise location of the microramp trailing edge
X_0	=	streamwise location of the inviscid shock reflection point
Y	=	wall-normal distance
Y^+	=	wall distance in law-of-the-wall coordinates
Z	=	spanwise distance from the tunnel centerline
α	=	microramp half-angle
δ	=	boundary-layer thickness
δ^*	=	incompressible boundary-layer displacement thickness
θ	=	incompressible boundary-layer momentum thickness

I. Introduction

SUPERSONIC intakes must provide a stable, uniform, low-loss, subsonic flow to the engine face at all flight conditions. Because of the excessive shock losses incurred by pitot intakes, mixed-compression intakes (see Fig. 1) are desirable for Mach numbers greater than 2 [1]. Oblique shock waves are an efficient form of compression; however, they interact with the boundary layer forming on the intake walls. The shock-induced adverse pressure gradient can trigger large-scale separation, resulting in significant total pressure loss and flow distortion. Furthermore, the unsteady aspects of separated shock-wave/boundary-layer interactions can cause large structural loads and may even lead to inlet unstart. It is therefore beneficial to control the flow either before or during the interaction process. The target of control is to prevent shock-induced separation, thereby improving efficiency and reducing distortion.

Boundary-layer bleed is the conventional form of flow control: low-momentum fluid is removed through a porous intake surface. However, the bled air is usually dumped overboard, which reduces the engine mass flow rate, leading to increased intake size for a given engine mass flux. This incurs an additional ram air drag penalty as well as weight penalties and increased system complexity. Reducing or eliminating bleed and its associated ducting will allow the intake frontal area to be reduced, which improves overall efficiency. Eliminating bleed, while maintaining intake performance, can therefore greatly increase aircraft range.

Conventional vortex generators (VGs), of a height of the order of the boundary-layer thickness, have been used for some time to provide flow control in supersonic applications (see, for example, Pearcey [2]). More recently, attention has been turned to smaller *sub-boundary-layer VGs* (SBVGs), with a height of approximately 40% of the boundary-layer thickness, that extend beyond the viscous sublayer [3–6]. It has been observed that SBVGs can reduce the boundary-layer shape factor, making it more robust and hence less susceptible to separation. The principal benefit of SBVGs compared with conventional VGs is their reduced drag. A further advantage is that the vortices of counter-rotating devices can remain in the boundary layer for a significant streamwise distance, whereas those of VGs often lift off the surface more quickly. A particularly attractive quality of microramps compared with other SBVGs is their physical robustness: intake manufacturers are unwilling to use fragile vortex generators, such as microvanes, that may break away during service, causing engine damage upon ingestion. Interest in microramps has been initiated by Anderson et al. [7], for which the Reynolds-averaged Navier–Stokes calculations suggest that the flow control afforded by microramps can have considerable benefits in supersonic inlets.

II. Experimental Setup and Measurement Accuracy

Experiments have been performed in a blowdown supersonic tunnel that is driven by a high-pressure reservoir and exhausts to atmosphere. All tests were conducted at a freestream Mach number of 2.5 and a nominal Reynolds number of 40×10^6 m^{-1}. The wind-tunnel stagnation temperature was set at 280 K (± 5 K) and the stagnation pressure was set to 380 kPa (the exact value is dependent on the amount of blockage generated by the experimental configuration and fluctuates by about 1% during a typical experiment). As a result of the variations in stagnation temperature

*Reader in Aerodynamics, Department of Engineering. Associate Fellow AIAA.
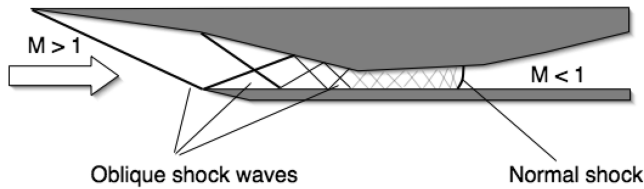†Research Student, Department of Engineering.

Fig. 1 Mixed compression supersonic intake.

and pressure, the freestream Reynolds number fluctuates by no more than 5%, which is sufficiently small to assume that the results are not affected. A compression ramp on the upper surface of the tunnel is lowered to generate an oblique shock wave. For all the experiments reported here, the wedge angle was set to 7 deg. The setup and key dimensions are shown schematically in Fig. 2. Note that streamwise distances are measured from the start of the working section, which is also the leading edge of the shock-generating wedge. In this coordinate system, the inviscid shock reflection takes place at $X = 159$ mm.

Geometrically similar microramps of four sizes (heights of 2, 3, 4, and 6 mm) have been tested (see Fig. 3). The microramps are scaled according to the specifications of Anderson et al. [7] so that the wedge half-angle α is equal to 24 deg, the side length c is 7.2 times the device height h, and the spanwise spacing s is 7.5 times h. Microramps were investigated individually as well as in arrays. The number of microramps in an array depended on their size. For the largest microramp (height of 6 mm), two devices were placed side by side; for the two intermediate sizes (4 and 3 mm), three devices were used; and for the smallest size (2 mm), five devices made up the array. All arrays were centered on the symmetry line. All microramps were located in the tunnel so that the trailing edges were aligned in the same streamwise position (regardless of wedge size), as seen in Fig. 2.

Flow visualization is carried out using a two-mirror schlieren system. The surface flow is visualized using a mixture of paraffin, titanium dioxide, and oleic acid. Diesel oil is added to this mixture to prevent it from drying before the flow was established.

One-component laser Doppler anemometry (LDA) was employed to determine profiles of streamwise velocity at various stations (see Fig. 2). The Dantec system in use featured a probe volume of 75 μm in diameter and approximately 2.5 mm in length (aligned in the spanwise direction). Seeding was obtained with oil droplets introduced in the settling chamber. The typical diameter of the seed particles was measured, using a commercially available TSI Scanning Mobility Particle Sizer, to be around 200 nm. The

combination of small probe volume and particle size allowed the determination of streamwise velocities down to a wall distance of 0.1 mm. Typically, at least 1000 samples were collected to calculate time-averaged velocities, and a weighting based on transit time was employed to remove velocity bias.

The traverse gear used for the LDA investigation was of greater accuracy than that used for probe-based measurements, giving uncertainties of less than 0.05 mm in the wall-normal direction. Because of the size of the probe volume, the uncertainty in the spanwise position is about 2.5 mm. Most of the LDA data were obtained along the centerline. However, some profile measurements were recorded offcenter, where the seeding density was lower. This has the effect of introducing noise into such LDA measurements (similar effects occur at large wall distances). When present, this is clearly seen in the data, and spikes resulting from this effect can be ignored. The accuracy of LDA data obtained in regions of good seeding is very high, especially for the time-averaged velocities shown here. Taking alignment errors and system uncertainties into account, average velocities are determined to better than 1% accuracy (except for regions of poor seeding). For the purpose of comparison of these data with computational fluid dynamics (CFD) predictions, it should be noted that the total temperature during a typical experiment varied by approximately 5 K. This introduces a corresponding variation of speed of sound that causes flow velocities to drift slightly during an experiment. Although not exactly an experimental error, this nevertheless introduces an effective uncertainty in velocity data of the order of 5 m/s in the freestream, making the total uncertainty of streamwise velocity 2% of the freestream value.

III. Results

A. Flow Development over Microramps (in the Absence of Shock Waves)

Figure 4 shows the velocity profile measured in an empty working section (no shock-generating wedge and no microramp) at $X = 89$ mm in physical (Fig. 4a) and log-law coordinates (Fig. 4b). The boundary layer is approximately 6 mm thick, and the (incompressible) integral values are displacement thickness 0.96 mm, momentum thickness 0.72 mm, and shape factor 1.32. The wall shear stress coefficient was estimated by fitting the velocity data to an analytical law-of-the-wall/wake profile suggested by Sun and Childs [8], giving a value of 0.0015. As can be seen from Fig. 4, there is a well-defined log region and the agreement with the analytical profile is excellent throughout. These results are typical for a naturally grown turbulent boundary layer in equilibrium.
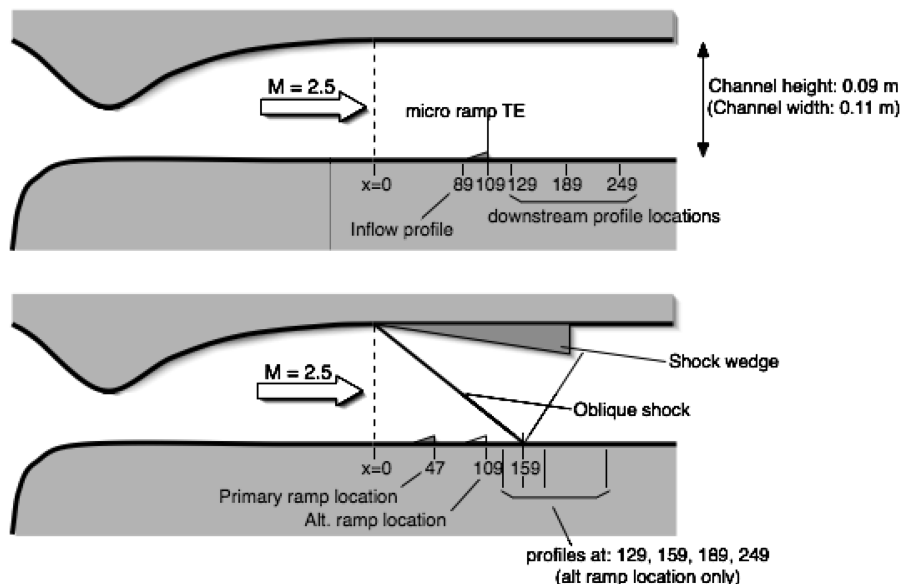

Fig. 2 Experimental setup for baseline experiments (top) and shock control experiments (bottom).
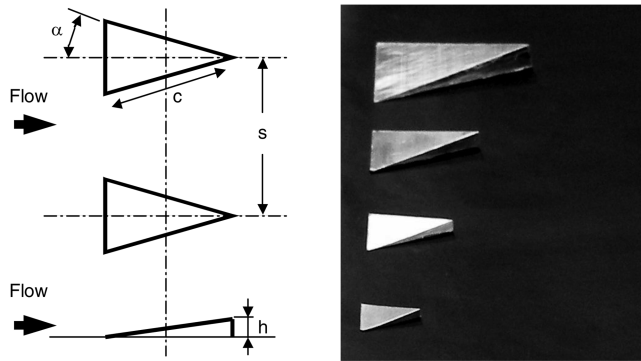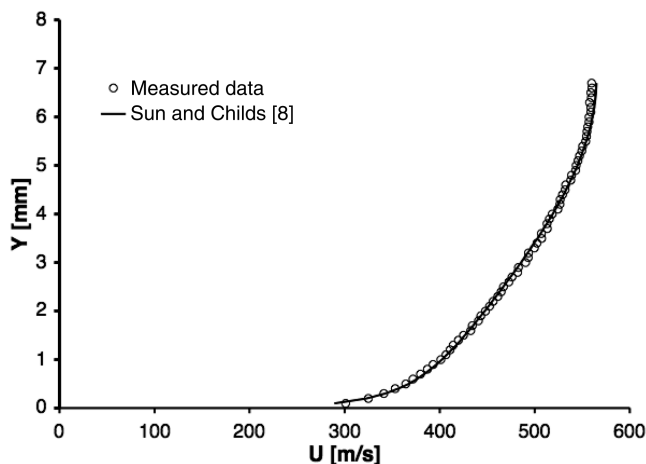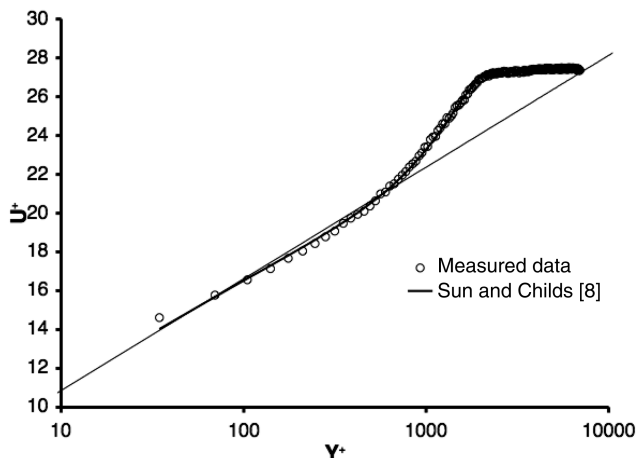
Fig. 3   Microramp geometry.

Figure 5 shows a schlieren image and surface oil-flow visualization of the flow over a microramp of 4 mm in height. In the schlieren photograph, the boundary-layer edge can be seen clearly and it is apparent that it is little affected by the presence of the device. Two oblique shock waves are seen to originate at the leading and trailing edges of the ramp. Less obvious is a faint near-horizontal edge downstream of the device that extends above the boundary layer. Later, it will be shown that this is the upper boundary of a low-momentum region.

The surface oil-flow pattern suggests a region of comparably high shear in the wake of the microramp, indicated by a darker color. At the upstream edge of the device there is an indication of a small

a) Schlieren photograph

b) Surface oil-flow visualization

Fig. 5   Flow visualization for 4 mm height microramp.

separation as the flow negotiates the compression ramp. This separation creates a very small horseshoe vortex for which the traces can also be seen on either side of the high-shear wake. The main feature of the wake region is the herringbone footprint of two primary (counter-rotating) vortices. Another feature is a small separation around the trailing edge of the ramp. Also seen are secondary vortices originating from the side-wall/floor junction of the ramp and separated from the primary vortices by separation lines. Note that there are two further secondary vortices originating from the top edges of the ramp, but these are not visible in the pictures. A schematic illustration of the various streamwise vortices is shown in Fig. 6 (only one-half of the symmetrical flowfield is shown for clarity). Close examination shows that the herringbone pattern fades some distance behind the ramp (of the order of 2 ramp lengths), suggesting that the primary vortices lift off the surface as a result of upwash induced by these vortices on each other.

Figure 7 compares the velocity profiles measured behind a 4-mm-high microramp at various spanwise locations (centerline, quarter-chord, semichord, and full span). The measurement location is 20 mm downstream from the trailing edge, which is about three-fourths of the ramp chord. The furthest outboard profile ($z = 12$ mm) is very similar to the undisturbed boundary layer. This is in agreement with the oil-flow visualization, which suggested that the effect of the ramps did not reach far beyond the span of the device. Nevertheless, this profile and all others exhibit increased velocities close to the surface, indicating high wall shear. Generally, the velocity profiles are fuller than the uncontrolled flow. However, the flow at the centerline features a pronounced low-velocity dip, which is the remnant of the device wake that has moved slightly away from the surface as a result of upwash from the primary vortex pair. The
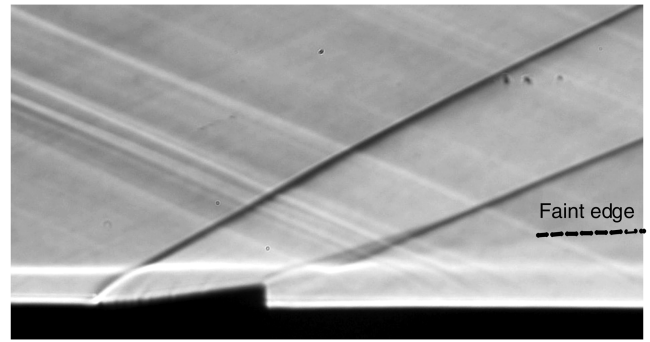

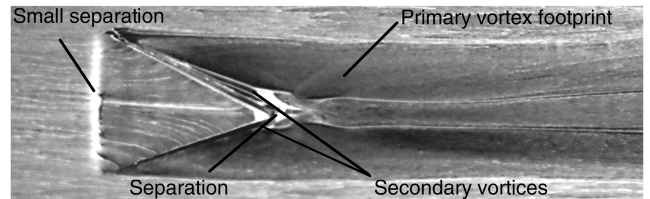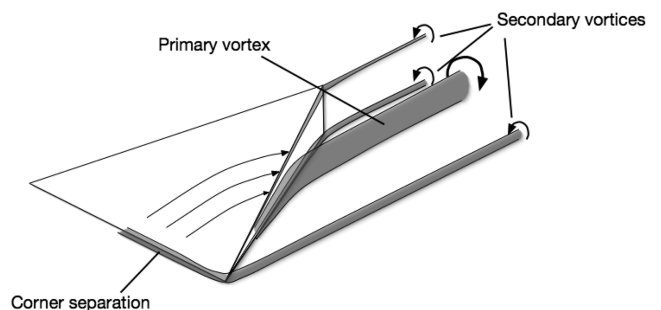a) Inflow boundary-layer profile

b) Inflow profile in law-of-the-wall coordinates

Fig. 4   Inflow boundary-layer profile (measured at $X = 89$ mm) and comparison with Sun and Childs [8] velocity profile.

Fig. 6   Sketch of main flow features (one side only for clarity).
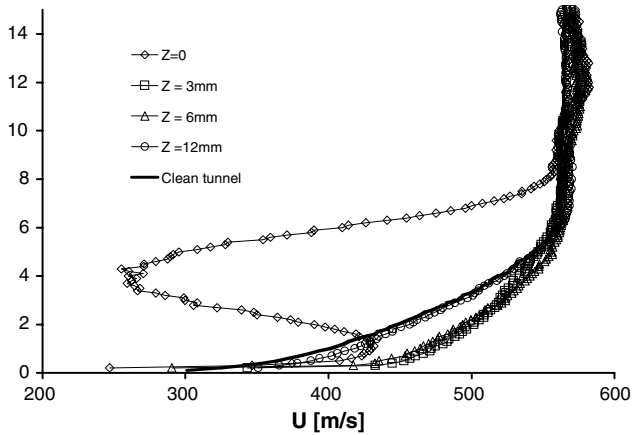
Fig. 7 Velocity profiles at $x = 129$ mm (20 mm downstream of ramp trailing edge) at various spanwise positions; 4 mm height microramp.
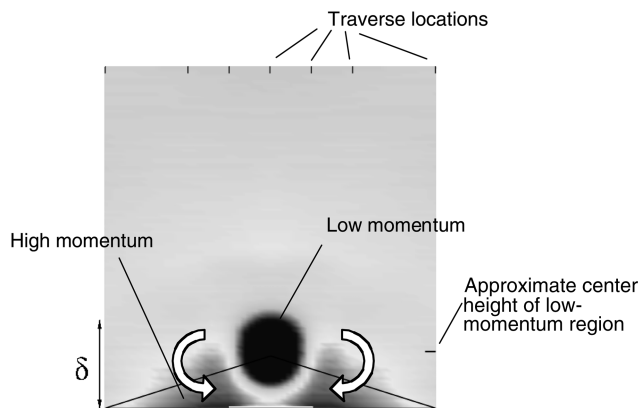

Fig. 8 Streamwise momentum difference between ramp flow and baseline velocity profiles. The outline of the microramp is indicated by thin lines for orientation.

upper edge of this dip is responsible for the faint edge seen above the boundary layer in the schlieren photographs.

The main features of the flow behind a microramp become more clear when shown in the form presented in Fig. 8. Here, the velocities measured behind the device are subtracted from the undisturbed velocity profile (recorded at the same location in the absence of

microramps). A number of spanwise profiles have been used and flow symmetry has been assumed to generate this image. The vertical bars at the top of the figure indicate when profile data were available, and the undisturbed boundary-layer thickness is indicated on the side of the image. Because the data presented in Fig. 8 have undergone significant processing, this image should be used for illustrative purposes only. In particular, it must be emphasized that the flow is not precisely symmetrical (as can be seen in surface the oil-flow images) and that the spatial accuracy is limited by the small number of traverse positions and the spanwise extent of the LDA probe volume. Nevertheless, regions of high momentum near the surface and the low-momentum dip are seen very clearly. Even at this relatively small distance downstream of the ramps, there is already a considerable entrainment of high-energy flow near the floor, covering almost all of the wake (except for a narrow region in the center). The low-momentum dip has begun to move away from the wall. The figure indicates the approximate location of the primary vortex pair and demonstrates the effect of these vortices on the entrainment of high-momentum fluid toward the surface and the movement of the low-momentum wake region. The flow evolution becomes clearer when considering Fig. 9, which combines velocity surveys recorded at three downstream distances. It can be seen that the low-momentum region is moved up and ejected from the boundary layer and high-momentum flow is distributed along the floor. By the last survey location, the relative strengths of the low- and high-momentum regions have begun to reduce through dissipation.

The size of the microramps has little effect on the fundamental flow features. This is illustrated by Figs. 10 and 11, which show flow visualizations for the smallest and largest devices tested (heights of 2 and 6 mm). The main flow features are almost identical to those described earlier for the 4 mm device.

A more detailed comparison of the effect of device height is shown in Fig. 12. This shows the momentum difference at three streamwise stations downstream of each device for all sizes. The exact locations of each traverse are as indicated in Fig. 2 (top). The data shown in Fig. 12 demonstrate that the flow development downstream of microramps is similar for all device heights. In each case, the low-momentum wake is gradually moved away from the wall by the action of the two primary vortices. Simultaneously, high-momentum fluid is entrained to the near-wall region by the same mechanism. Closer inspection of this figure, however, suggests that the speed with which these processes occur is not the same across the devices. For example, in the first downstream profile ($X = 129$ mm) behind the largest device (6 mm) there remains a considerable region of low momentum close to the floor around the symmetry plane. At the same
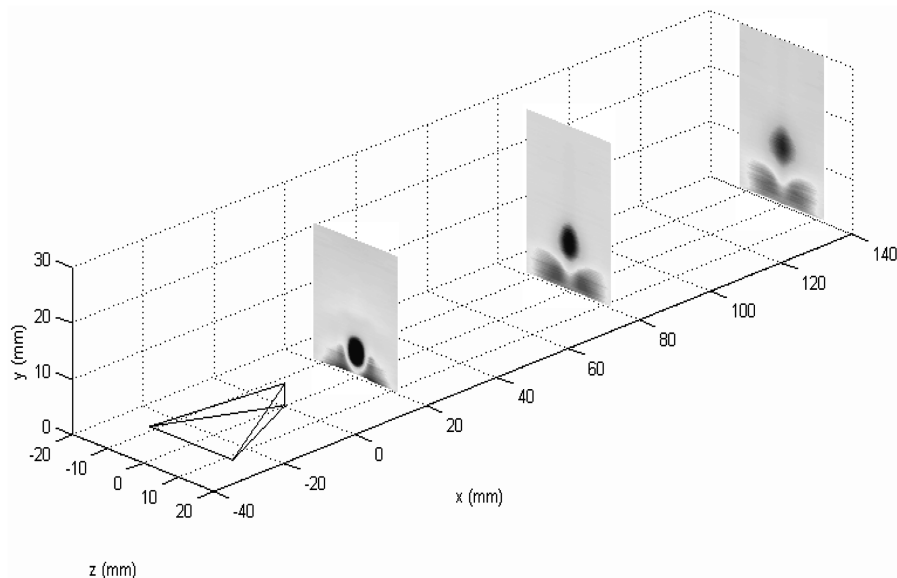

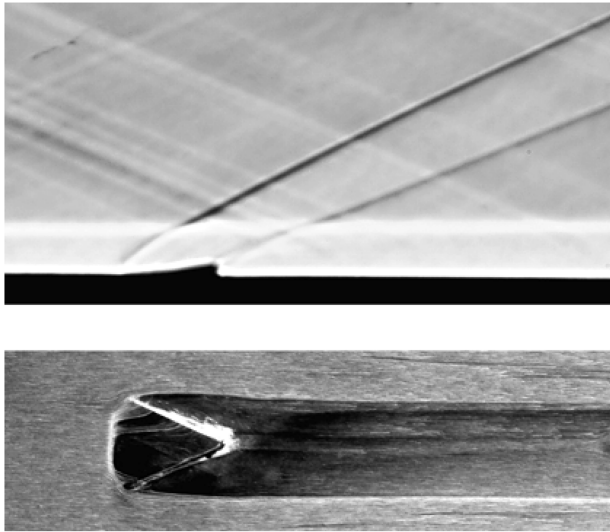**Fig. 9 Streamwise flowfield development.**

Fig. 10 Schlieren photograph and surface oil-flow visualization for flow over a 2 mm microramp.
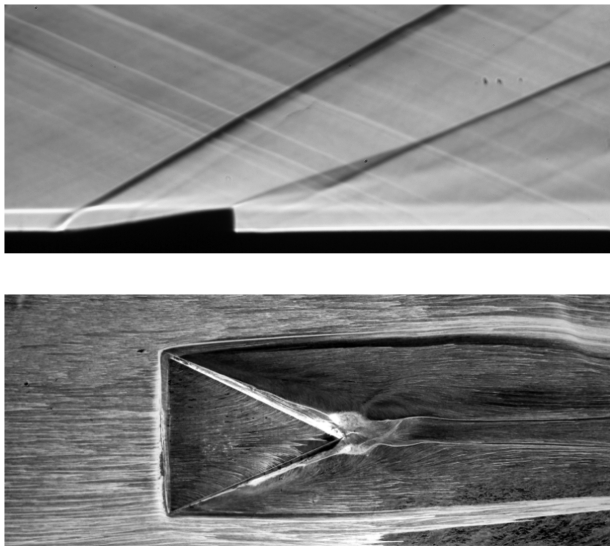

Fig. 11 Schlieren photograph and surface oil-flow visualization for flow over a 6 mm microramp.
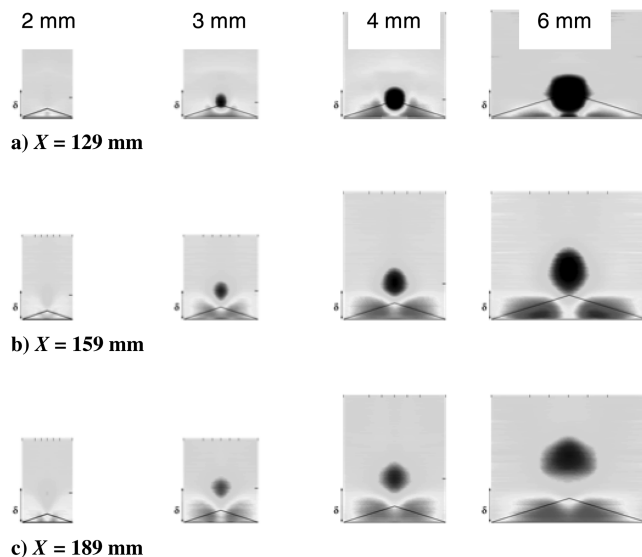

a) $X = 129$ mm

b) $X = 159$ mm

c) $X = 189$ mm

Fig. 12 Streamwise momentum difference at various downstream locations for all devices tested.

downstream location behind the much smaller 3 mm device, however, the same area is already filled with high-momentum fluid. This stage of development is only reached much later behind the largest device.

This observation suggests that the flow development, although similar, does vary with device height. To test this hypothesis, the approximate height of the center of the low-momentum region is estimated from each of the subplots seen in Fig. 12. The result is given in Fig. 13 in nondimensional form; that is, both the height above the surface as well as the streamwise distance from the device are divided by the device height. It should be noted that the first data point for the 2 mm device is subject to considerable error because it was not possible to identify the low-momentum region properly.

It can be seen that the nondimensional flow evolution collapses on one line for all cases (excluding the first point for $h = 2$ mm). This would suggest that the flow development behind microdevices may indeed scale with device height. A similar conclusion was reached by Ashill et al. [6] based on experiments performed on micro VGs in incompressible flow. This suggests that the flow behind smaller devices evolves more quickly than that generated by larger devices. High momentum is moved to the near-wall regions more quickly, and in a practical application it would therefore be advisable to move smaller devices closer to the region requiring control.

The data presented in Fig. 12 also suggest that larger devices incur a greater low-momentum wake (in extent and magnitude), and the vortices generated by bigger devices are larger, more intense, and further from the surface. Although greater vortex intensity is clearly helpful for control purposes, this is achieved at the cost of additional device drag. Also, smaller devices may have a disproportionately beneficial effect on the boundary layer because the generated vortices are better positioned to entrain high-momentum fluid into the near-wall region.

B. Effect of Microramps on Reflected Shock-Wave Interactions

Figure 14 shows a schlieren photograph and surface oil-flow visualization for the baseline uncontrolled interaction. It can be seen that the flow along the floor exhibits a short region of separation, with a streamwise extent of approximately three incoming boundary-layer thicknesses. Significant sidewall and corner effects are present and the flowfield should therefore be considered to be three-dimensional. Figure 15 shows the surface pressure measured along the tunnel centerline and at a spanwise position approximately halfway between the centerline and the side wall. It can be seen that although the near-wall flow is clearly three-dimensional, the surface pressure rise across the interaction is almost uniform across the span.

Microramps were tested individually as well as in the spanwise arrays (spacing as shown in Fig. 3). In all cases, microramps were placed 112 mm ahead of the nominal shock reflection point (see Fig. 2). In nondimensional terms, this is between 19 and 56 device heights (depending on the size of microramp). Comparison of these dimensions with the data shown in Figs. 12 and 13 would suggest that, in all cases, the primary vortices will have lifted off the surface
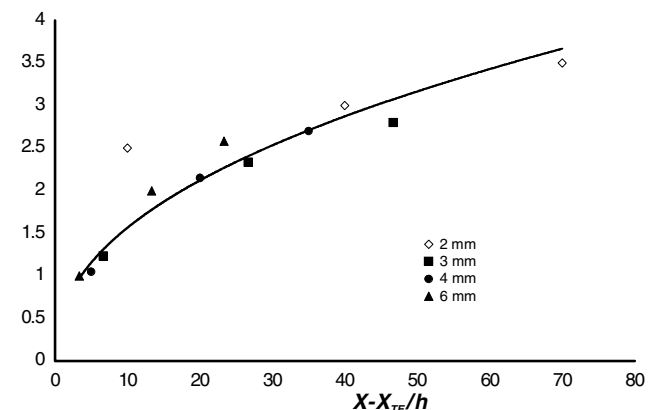

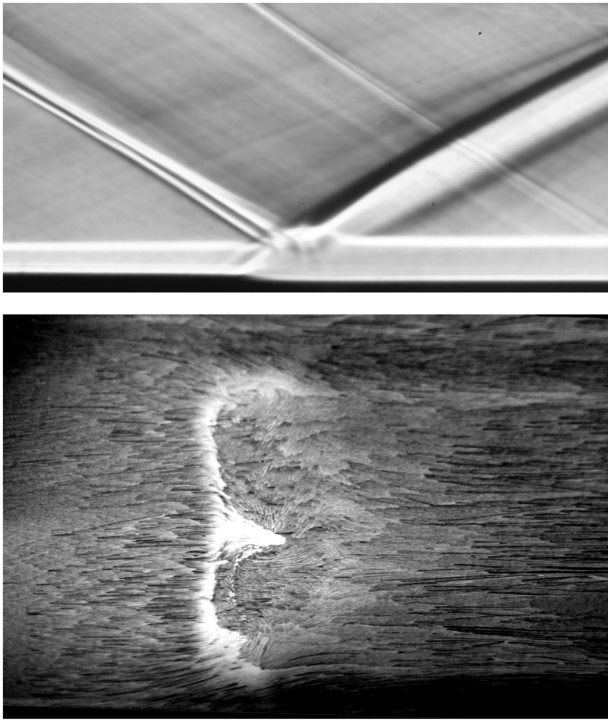**Fig. 13 Nondimensional height of low-momentum region (from Fig. 10) as a function of the distance from the device.**

Fig. 14 Schlieren photograph and surface oil-flow visualization for oblique shock reflection (7 deg wedge angle).
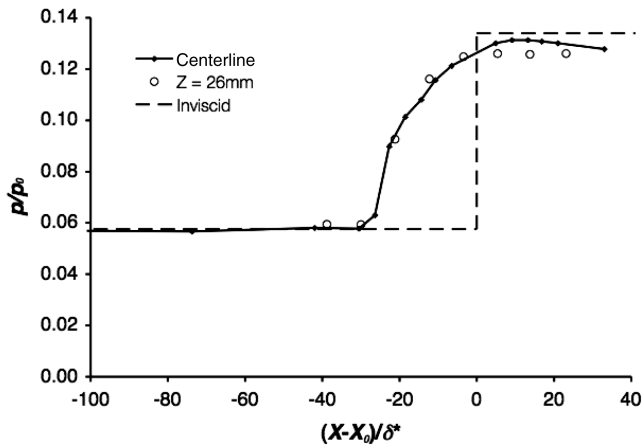

Fig. 15 Surface pressure distribution through uncontrolled baseline interaction along the centerline and offcenter.
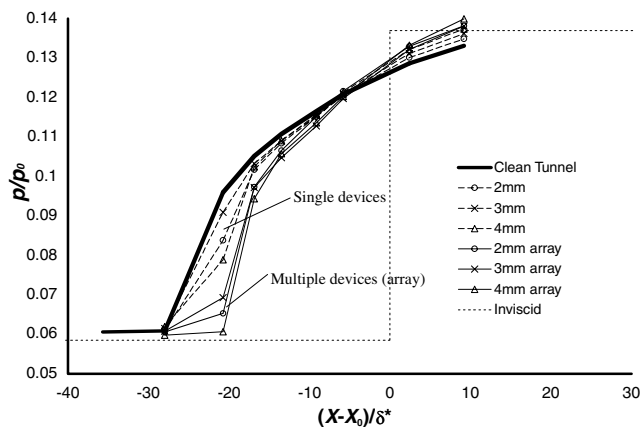

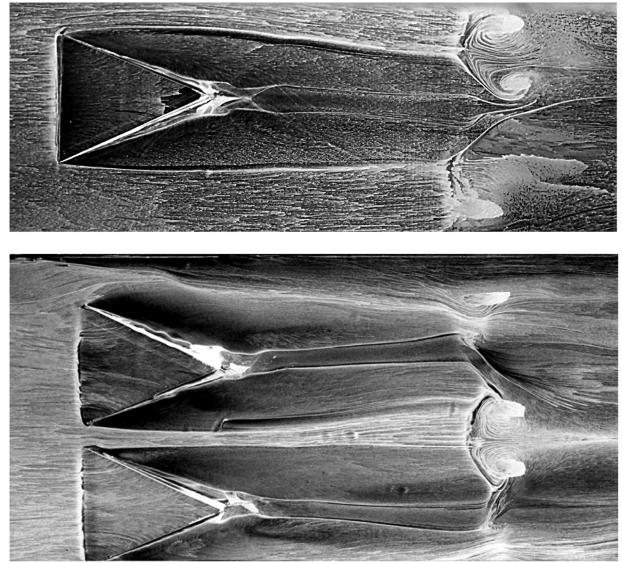**Fig. 16 Centerline surface pressure distribution through interaction with and without control.**

Fig. 17 Surface oil-flow visualization for oblique shock-wave/ boundary-layer interactions controlled by single 6 mm microramp (top) and array of two 6 mm microramps (bottom). In both cases, the separated region is broken up into a cellular structure.

and that the entrainment of high-momentum fluid into the near-wall region is well advanced before the adverse pressure gradient is encountered. It can be seen in Fig. 16 that all devices reduced the upstream influence and increased the pressure gradient, which suggests a reduction of separation. Arrays of devices performed significantly better than single ramps and greater ramp heights proved to be slightly more effective.

Figure 17 shows typical surface oil-flow visualizations obtained for oblique shock reflections controlled by microramps. It can be seen that the presence of microramps causes a small region of attached flow in its immediate wake (approximately behind the device centerline). This has the effect that the separated flow is broken up into a number of individual cells of three-dimensional separation. When multiple devices are placed in an array, the number
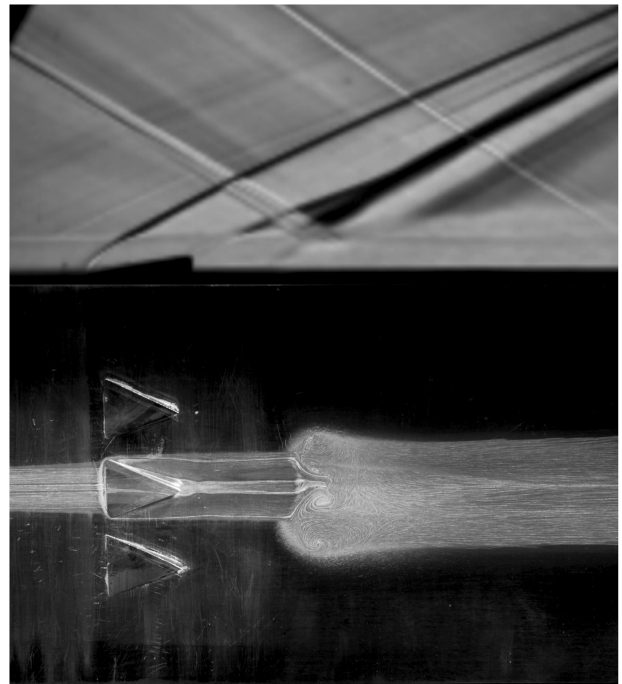

Fig. 18 Schlieren photograph and surface oil-flow visualization for an array of 3 mm microramps placed 50 mm upstream of the nominal shock reflection location. Note that only the center region is covered in oil.
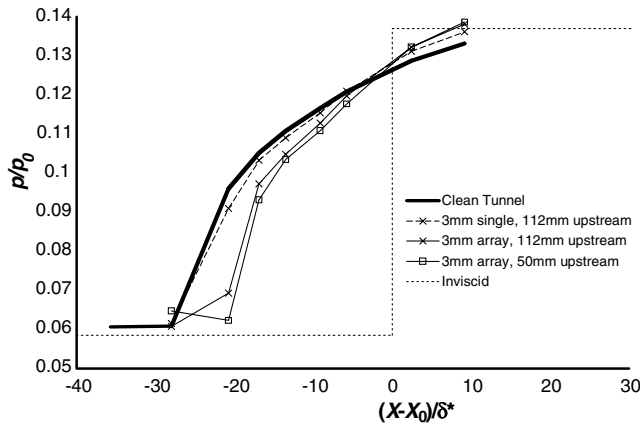
Fig. 19 Centerline surface pressure for interaction controlled with 3 mm devices at two streamwise locations.

of cells increases in line with the number and placement of the ramps. Although the presence of microramps cannot eliminate separation completely, there is a reduction of the overall size of the separated region, which is in line with the observations from the pressure measurements.

The effect of streamwise placement relative to the interaction was also investigated. Figure 18 shows a schlieren photograph and surface oil-flow visualization obtained for an array of 3 mm microramps placed closer to the location of interaction. Here, the distance between the trailing edge and the inviscid shock impingement point was 50 mm, which is 16.7 device heights (see Fig. 2). Comparison with Figs. 12 and 13 would suggest that at this distance, the primary vortices have lifted off the surface and that high-momentum fluid has been entrained throughout the near-wall region. However, in practice, the actual interaction region lies significantly upstream of the inviscid reflection point and the effective distance is therefore much shorter. This is confirmed by the

surface oil-flow visualization (Fig. 18) and the surface pressure distribution (Fig. 19), which show the interaction region starting well ahead of the inviscid reflection point. In effect, this places the device much closer to the interaction region, at about a quarter of the previous effective distance. Nevertheless, it can be seen that the effect of the devices on the separation is quite similar to that observed for larger distances. The separation is broken up into cells but not eradicated.

Figure 19 compares the centerline surface pressures measured for the two device locations. It can be seen that there is little difference, although the closer placement appears to have a slightly stronger effect on the interaction, giving a slightly shorter upstream influence and a steeper pressure rise. The relative similarity in the control effect for both device locations suggests that either the optimum location is somewhere in between the two positions or that streamwise position is not a very sensitive parameter.

Figure 20 compares velocity profiles measured across the interaction for the configuration seen in Figs. 18 and 19. Profiles were recorded at four streamwise positions (see Fig. 2). In each location, profiles were also recorded at various spanwise stations relative to the central device (centerline, half-span, and full span). Some of the data in the outer regions of the boundary layer suffer from noise due to poor seeding quality. However, the near-wall region is well resolved in all cases. Integral boundary-layer quantities obtained at the extreme spanwise position suffer from additional errors due to this noise, and so they should be seen as qualitative only.

When microramps are present, the velocity profiles recorded along the centerline show evidence of the low-momentum wake discussed earlier. This wake is seen to move away from the wall with downstream distance and to persist throughout the shock interaction. Elsewhere, the velocity profiles are significantly fuller and the boundary-layer thickness is reduced compared with the uncontrolled case. This is illustrated by Fig. 21, which shows the development of the incompressible boundary-layer displacement thickness and shape factor across the interaction. Apart from the data recorded on the centerline, which are affected by the low-momentum wake, all

a) X = 129 mm

b) X = 159 mm
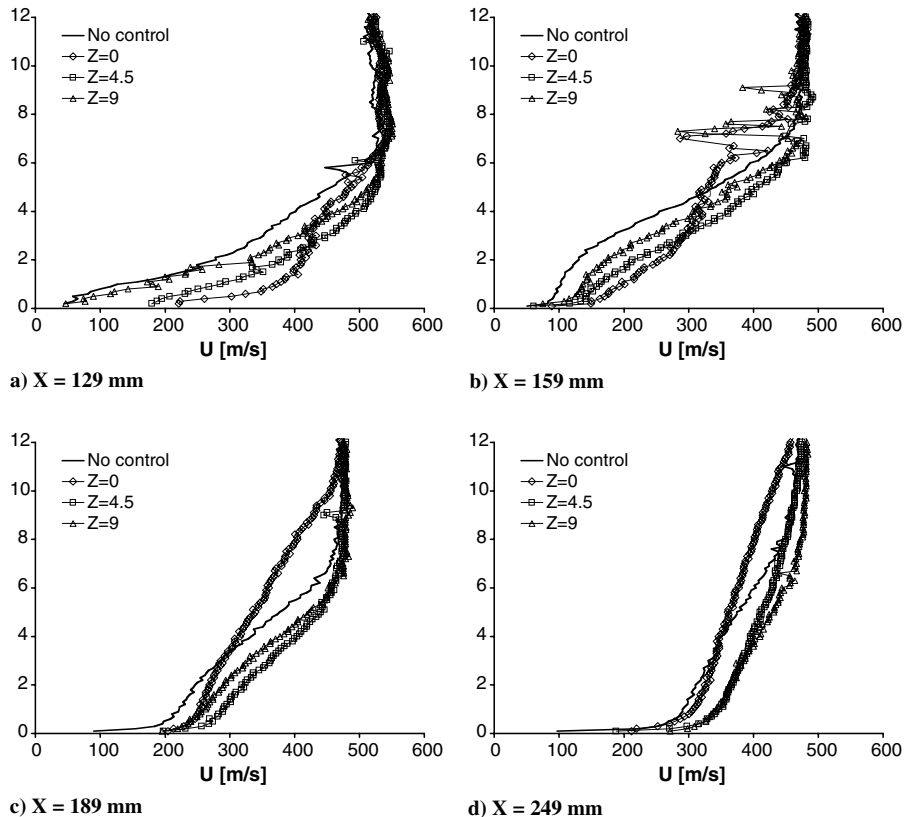
c) X = 189 mm

d) X = 249 mm

Fig. 20 Streamwise velocity profiles measured with LDA at various streamwise and spanwise stations for the interaction controlled by an array of 3 mm microramps located 50 mm upstream of the nominal shock reflection location: a) displacement thickness and b) shape factor.
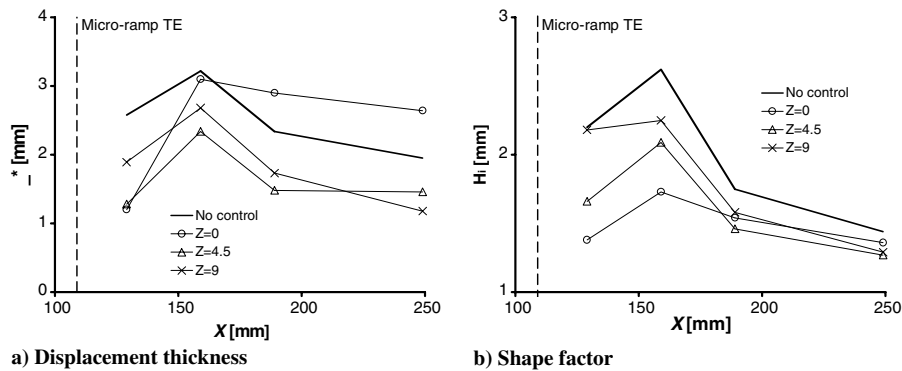
a) Displacement thickness   b) Shape factor

Fig. 21   Streamwise development of boundary-layer displacement thickness and shape factor.

boundary layers are considerably thinner. The incompressible shape factor, which is a good measure of boundary-layer health, is significantly improved throughout the flowfield. These observations confirm the beneficial action of microramps and suggest that they are able to improve the flow over some spanwise distance. However, the optimum spanwise spacing of such devices has not yet been determined and is subject to future research.

IV.   Conclusions

The flow over microramps has been characterized with detailed measurements and flow visualizations. The information gathered is valuable for the understanding of microramp flows as well as for providing validation data for CFD simulations.

Downstream of the microramps, a relatively complex structure of multiple pairs of counter-rotating streamwise vortices is observed. Around the centerline behind the ramp, a significant low-momentum region is formed as a consequence of viscous drag of the device. The extent and magnitude of this low-momentum wake increase with device size. The wake flow is dominated by two counter-rotating primary vortices that act to entrain high-momentum fluid from the outer regions of the boundary layer toward the surface. Simultaneously, the low-momentum wake is transported away from the surface to be eventually deposited outside the boundary layer at some downstream distance from the device. The development of the vortical flow in the wake of microramps can have subtle but important effects regarding the positioning of low- and high-momentum flow regions. The exact locations of high- and low-momentum fluids are thought to be important for the devices' ability to prevent flow separation, and it is therefore believed that numerical simulations need to be able to capture these effects correctly.

No fundamental change of the flow structure was observed with different microramp sizes (heights from 30–100% of boundary-layer thickness). The results shown here suggest that the flow development can be scaled geometrically with device height.

Microramps of all sizes were found to reduce separations in a $M = 2.5$ oblique shock reflection by breaking up a previously two-dimensional separation region into cells of separated flow (surrounded by attached flow). Arrays of multiple devices distributed across the span had a much more beneficial effect than individual devices.

The largest ramp size tested was found to have the strongest effect; however, it also incurred the greatest momentum deficit (i.e., drag). The smallest device height was able to have almost similar beneficial effects without incurring significant device drag. This would suggest

that smaller device sizes are more advantageous in an application. It can be hypothesized that there is a minimum size for effective flow control, but this minimum has not been reached in the present study.

No significant effects were observed when changing the device location relative to the shock reflection region; however, all locations tested were quite close to the interaction region. It is thought that microdevices should be placed closer to adverse pressure gradients than traditional vortex generators and that the optimum location is likely to be a function of device height.

References

[1] Seddon, J., and Goldsmith, E. L., *Intake Aerodynamics*, 2nd ed., Blackwell Science, Boston, 1999.

[2] Pearcey, H., "Boundary Layer Control for Aerofoils and Wings," *Boundary Layer and Flow Control: Its Principles and Application*, Vol. 2, edited by G. Lachmann, Pergamon, Oxford, 1961.

[3] McCormick, D. C., "Shock/Boundary-Layer Interaction Control with Vortex Generators and Passive Cavity," *AIAA Journal*, Vol. 31, No. 1, Jan. 1993, pp. 91–96.
doi:10.2514/3.11323

[4] Holden, H. A., Babinsky, H., "Effect of Microvortex Generators on Separated Normal Shock/Boundary Layer Interactions," *Journal of Aircraft*, Vol. 44, No. 1, Jan.–Feb. 2007, pp. 170–174.
doi:10.2514/1.22770

[5] Lin, J. C., "Review of Research on Low-Profile Vortex Generators to Control Boundary-Layer Separation," *Progress in Aerospace Sciences*, 2002.

[6] Ashill, P. R., Fulker, J. L., Hackett, K. C., "A Review of Recent Developments in Flow Control," *The Aeronautical Journal*, Vol. 109, No. 1095, May 2005, pp. 205–232.

[7] Anderson, B., Tinapple, J., and Surber, L., "Optimal Control of Shock Wave Turbulent Boundary Layer Interactions Using Micro-Array Actuation," AIAA Fluids Engineering Conference, San Francisco, AIAA Paper 2006-3197, June 2006.

[8] Sun, C. C., and Childs, M. E., "A Modified Wall Wake Velocity Profile for Turbulent Compressible Boundary Layers," *Journal of Aircraft*, Vol. 10, 1973, pp. 381–383.
doi:10.2514/3.44376